Proton radiography of cylindrical laser-driven implosions

2011 Plasma Phys. Control. Fusion 53 032003

(http://iopscience.iop.org/0741-3335/53/3/032003)

Plasma Phys. Control. Fusion **53** (2011) 032003 (9pp) doi:10.1088/0741-3335/53/3/032003

BRIEF COMMUNICATION

Proton radiography of cylindrical laser-driven implosions

L Volpe[1], R Jafer[1], B Vauzour[2], Ph Nicolai[2], J J Santos[2], F Dorchies[2], C Fourment[2], S Hulin[2], C Regan[2], F Perez[3], S Baton[3], K Lancaster[4], M Galimberti[4], R Heathcote[4], M Tolley[4], Ch Spindloe[4], W Nazarov[5], P Koester[6], L Labate[6], L A Gizzi[6], C Benedetti[7], A Sgattoni[7], M Richetta[8], J Pasley[9], F N Beg[10], S Chawla[10], D P Higginson[10], A G MacPhee[11] and D Batani[1]

[1] Università di Milano-Bicocca, Italy
[2] CELIA, Université de Bordeaux, CNRS, CEA, F33405, France
[3] LULI, Ecole Polytechnique-CNRS-UPMC, 91128 Palaiseau Cedex, France
[4] RAL, STFC, UK
[5] St. Andrews University, UK
[6] INO-CNR, Pisa, Italy
[7] University of Bologna, Italy
[8] University of Rome 'Tor Vergata', Italy
[9] Department of Physics, University of York, York, YO10 5DD, UK
[10] University of California San Diego, UCSD, USA
[11] LLNL, USA

Received 3 November 2010, in final form 22 December 2010
Published 3 February 2011
Online at stacks.iop.org/PPCF/53/032003

Abstract
We report on the results of a recent experiment at the Rutherford Appleton Laboratory investigating fast electron propagation in cylindrically compressed targets; a subject of interest for fast ignition. This experiment was performed within the framework of the road map of HiPER (the European High Power laser Energy Research facility Project). Protons accelerated by a ps-laser pulse are used to radiograph a 220 μm diameter, imploded with ~200 J of laser light (1 ns $\lambda = 0.53\,\mu$m) in four symmetrically incident beams. Results are also compared with those from hard x-ray radiography. Detailed comparison with 2D radiation hydrodyamics simulations is performed with the aid of a Monte Carlo code adapted to describe plasma effects. Finally, a simple analytical model is developed to estimate the performance of proton radiography for given implosion conditions.

(Some figures in this article are in colour only in the electronic version)

1. Introduction

Many diagnostics [1] have been used in Inertial Confinement Fusion (ICF) related experiments to follow the implosion dynamics, including proton radiography (PR) [2–4]. Laser-based proton sources have been used in this context, in particular for small-scale experiments performed in the framework of the fast ignition approach to ICF [5]. Here the evolution of targets is imaged using the relatively low-energy (∼10 MeV) protons created by the interaction of high intensity (10^{18}–10^{21} W cm^{-2}) lasers with solid targets. In this context, an experiment has been performed at the Rutherford Appleton Laboratory (RAL) in the framework of the HiPER roadmap [6] with the goal of studying the transport of fast electrons in cylindrically compressed matter [7, 8]. In the first phase of the experiment PR is used, together with hard x-ray radiography, to record the implosion history of a cylindrical target. Laser-produced protons are characterized by small source, high degree of collimation and short duration. The broad proton energy spectrum allows for probing the implosion at different times in a single shot, due to the spread of proton time of flight across the spectrum. PR with laser-produced protons, and radiochromic films (RCF) as detectors, has previously been employed [4, 5] to probe the implosion of a spherical shell. Here, experimental results were analyzed and compared with Monte Carlo (MC) simulations. The analysis straightforwardly related proton energy to Bragg peak deposition depth and time of flight. This approach has proven to be very successful in the detection of electric and magnetic fields in plasmas [9, 10]. Using this methodology, Mackinnon *et al* [4] associate each RCF layer with a given probing time. Most of their analysis is performed based upon an image of the imploding shell obtained in the layer corresponding to the Bragg peak for 7 MeV protons (∼1 ns before stagnation). They observe significant differences between the shell size predicted by hydro codes (85 μm) and the size recorded on RCF images (120 μm), and justify this difference on the basis of the scattering of protons in the compressed core and the presence of electric and magnetic fields affecting proton trajectories providing a questionable interpretation of results. In this paper, we seek to demonstrate that similar discrepancies are mainly caused by the fact that, as protons are penetrating thick and dense targets, they suffer severe multiple scattering (MS) effects and energy losses. These effects have previously been considered in static PR by Roth *et al* [13], but acquire a deeper meaning in our dynamic situation, leading to mixing of the images formed by protons of different energies. This implies that a more careful analysis of RCF images is needed than simple layer-to-time correspondence, and suggests that detailed comparison with computer simulations is required. Experimental results were compared with simulations performed with the MC code MCNPX [11] using the 2D density and temperature profiles of the imploding cylinder obtained with the 2D Lagrangian radiation hydrodynamics simulation code CHIC [12]. Whenever such analysis is done, we obtain good agreement between experimental results and hydro simulations without the need to rely upon the presence of any additional effects. We also show that the large extension of the low-density plasma corona plays a crucial role in image formation, which is inconsistent with the interpretation presented in [4].

2. Experimental setup

The experiment is carried out using four long-pulse (LP) beams of the Vulcan laser beams to drive the implosion of a cylindrical target. The beams (∼4 × 50 to 4 × 70 J in 1 ns) at 0.53 μm, are focused to 150 μm FWHM spots (figure 1). A short pulse beam (SP) (100–150 J in 1 ps at $\lambda = 1.064$ m) is focused on a 20 μm gold foil by an $F = 3.5$ off axis parabola with a focal spot of 20 μm FWHM and a peak irradiance of 1.5×10^{19} W cm^{-2} to produce protons for radiography. An intense beam (10 ps 160 J) is focused on a 25 μm titanium foil providing the

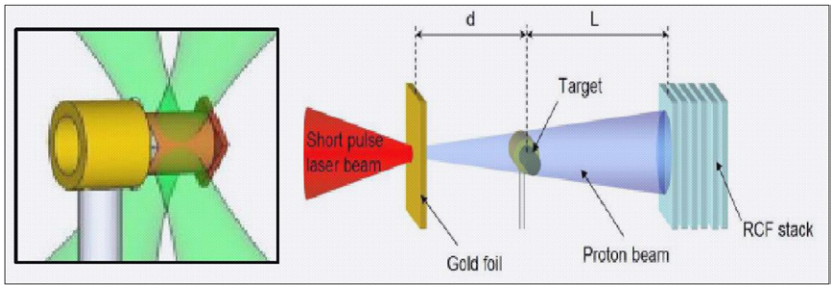

Figure 1. (left) Schematic of the four compression beams (each of 1 ns) focused on the plastic cylinder. (right) Proton radiography setup.

source for hard x-ray radiography at $h\nu \approx 4.5$ keV (see [8]). The target comprises a 200 μm-long polyimide cylindrical tube with 220 μm outer diameter and 20 μm wall thickness which in some cases is filled with a plastic foam (acrylate) at a density of either 0.1 or 1 g cm^{-3}. One end of the cylinder is sealed with a Cu foil and the other with a Ni foil. The four LP beams simultaneously illuminate the cylinder (jitter $\pm$50 ps). The delay between LP and SP is adjustable from 0 to 3.6 ns. Protons are produced by interaction of the SP with a 20 μm gold foil and have an approximately exponential spectrum with a cut-off energy of $\sim$10 MeV. The proton detector consists of a multilayer film stack containing radiochromic film (RCF; types: MD-55 and HD-810) (see figure 1(*b*)) The measured optical density on each RCF active layer is proportional to deposited energy [14] allowing for the reconstruction of the proton spectrum. In particular [15], the energy deposited in each RCF layer is given by the convolution of the energy deposition function (characterized by the presence of the Bragg peak) and the proton energy distribution. The initial spectrum of the proton beam is determined as in [3] with uncertainties derived from shot-to-shot variations in energy and angular distribution of the emitted protons.

3. Experimental analysis

The experimental arrangement is shown in figure 1. The images recorded on RCF were digitized with a Nikon 4.0 scanner with 4000 dpi resolution ($\sim$6.5 μm). The geometrical magnification, M, is 4.5 allowing a spatial resolution of $\sim$1.5 μm. Typically seven of RCF layers are exposed per shot, covering a full time span of 500 ps. Therefore it is not possible to follow the complete target implosion in a single shot. Changing the delay between the SP and LP allows reconstruction of the full implosion history with multiple shots (typically 3). Examples of experimental radiographs of the cylinder both before and during compression are shown in figure 2 (above). Compression along the longitudinal direction (cylinder axis) is not uniform. This is due to the limited size of the LP focal spots compared with the cylinder length. However, the focal spots are large enough that 3D effects can be neglected. For each RCF image the optical density profile in the radial direction (dashed white line in figure 2) is extracted, and a FWHM evaluated, corresponding to the diameter of the cylinder in-flight. The optical density profile is approximately super-Gaussian at early times (including the initial cold cylinder), approaching a Gaussian around the stagnation time.

This reflects the transition from a sharp cylinder boundary at early times to an extended plasma corona later. The measured widths are compared with the diameter of the compressed cylinder obtained from CHIC, which assumed no variation of the intensity along the

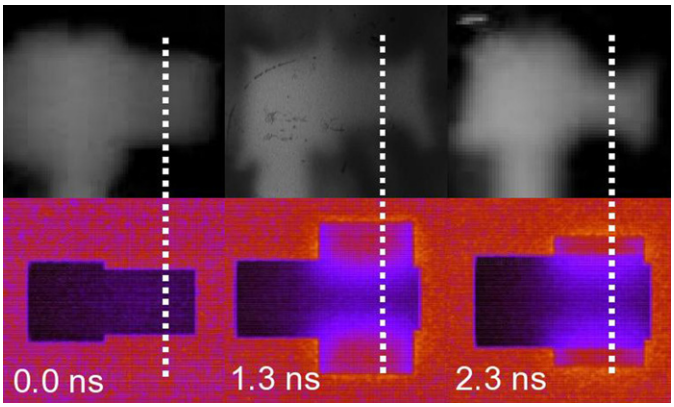

Figure 2. 2D images of the cylinder compression history obtained (above) by analysis of experimental PR and (below) by MC simulations (starting from density profiles simulated using hydrodynamic code CHIC) at $t_1 = 0$ ns, $t_2 = 1.3$ ns, $t_3 = 2.3$ ns.

longitudinal direction. Note that the compression is not uniform in the polar direction either, as a consequence of the small number of LP beams (only four). This implies a different target compression at 0° (direction of one of the LP beams) and at 45° (observer direction exactly between two LP beams), an effect which is taken into account by performing 2D simulations.

Figure 3 shows the time evolution of the cylinder diameter compared with the numerical prediction from the hydro simulations for the case of a cylinder filled with 0.1 g cm^{-3} foam. It clearly shows the trend of compression of the target and it also reproduces the stagnation time given by simulations quite well (∼2.1 ns). Note that the estimate of the stagnation time is obtained running different MC simulations for each hydro profiles relative to different laser energies (stagnation time is a strong function of driver energy) and choosing the best fit with experimental data. It is clear, however, that the absolute value of the diameter of the compressed cylinder is not reproduced. In particular, the minimum observed diameter from PR is ∼140 μm. By comparison x-ray radiography yielded a minimum diameter of ∼80 μm [8] and in the CHIC results with comparable stagnation time this is reduced further to ∼50 μm. This suggests that the protons are not able to probe the dense core.

4. MC simulations

In order to investigate the physical basis of this result, Monte Carlo simulations are performed using the code MCNPX developed at LANL [9]. This can reproduce the experimental set-up in all its relevant parts: the proton source, target and detector. Stopping power (ST) of protons in the target is described using Bethe's theory [16] while MS effects are described by Rossi's theory [16]. In our experiment, there is a significant region (plasma corona) in which the temperature becomes high ($T \sim 1$ keV) implying a large number of free electrons with respect to the bound electrons and a corresponding enhancement of ST. These effects, which are a function of the density, temperature and ionization state of the target, must be taken into account when comparing simulations with experimental data. A number of theoretical studies on ion beam interaction with plasmas are found in the literature [17, 18] predicting an increased ion ST in ionized materials as experimentally observed in [18]. Conventional MC codes, such as MCNPX, FLUKA and SRIM, do not take into account such effects because they are developed for use with cold matter.

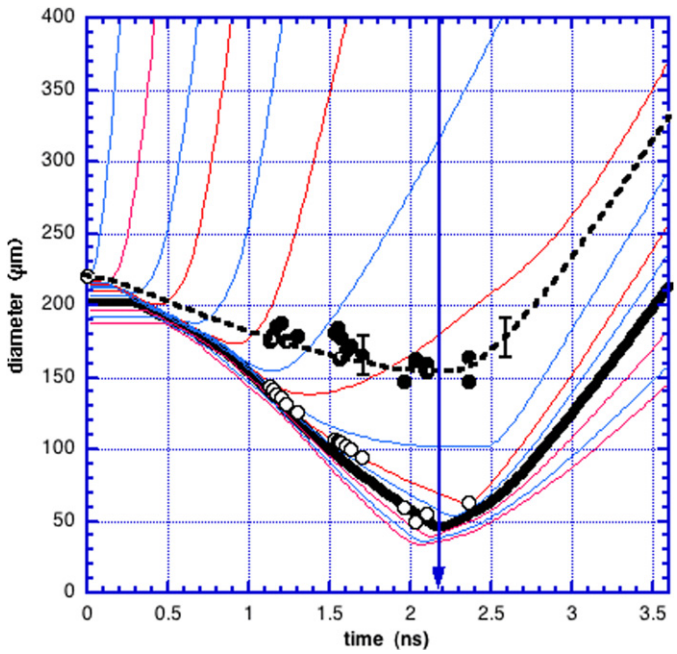

Figure 3. FWHM of the cylinder 1D profiles as a function of time Experimental (full circle) versus hydrodynamic simulations (empty circle). Continuous lines represent the hydrodynamic evolution of each point of the cylinder obtained running the CHIC code.

We include plasma effects in the code MCNPX by replacing the 'real' density profile given by hydro simulation with an 'effective' profile that gives the same degree of ST as is expected in the plasma [17].

The comparison between the FWHM obtained using both the original and effective density profiles is shown in figure 4. Simulations of the image formation are performed as follows: (i) We start from hydro profiles (density, temperature and mean ionization) at a given time point from the CHIC code output [12]. (ii) For each time point, we run a MC simulation calculating the energy deposition in each RCF layer. Each hydro-time corresponds to a different time of flight of the incoming protons, i.e. to a different proton energy. However, here we consider the energy deposited by such protons *in all* RCF layers and not only in the one corresponding to the Bragg peak of the *emitted* protons (of course, images will be formed only in RCF layers up to the one corresponding to the *initial* Bragg peak). (iii) The full time span is then covered by considering other time points in the simulation, and the corresponding energy of the incoming protons. Thus, for each RCF layer we get a series of mono-energetic, fixed-time, 2D images. (iv) Finally for each RCF layer, we sum all images at different times, each with a weight given by the energy spectrum of the proton beam. The resulting images on each layer will therefore comprise contributions from a range of time points as measured at the target and can be compared with the experimental ones (as shown in figure 2). Finally, the FWHM is extracted from the synthetic images in the same manner as for the experimental data. In agreement with the experimental observations, a transition from super-Gaussian profiles at early times to Gaussian ones later is observed. Note that the procedure for these synthetic image creation is implicitly 3D; however, the simulated compression is uniform in the direction of the cylinder axis. The effect seen at the edges of the compressed cylinder in figure 2 is therefore simply due

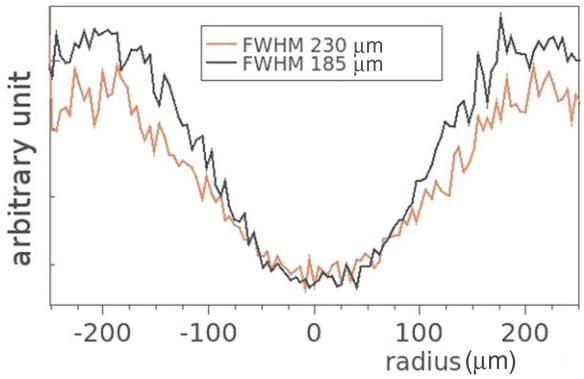

Figure 4. MC simulation of proton energy deposition in layer corresponding to the Bragg peak for $E_p = 3.2$ MeV unperturbed protons (MC simulation without cylinder between proton source and detector), taken from the original hydrodensity profile (above dark line on line) or using an effective density profile (plasma effects accounted for) (below red line on line).

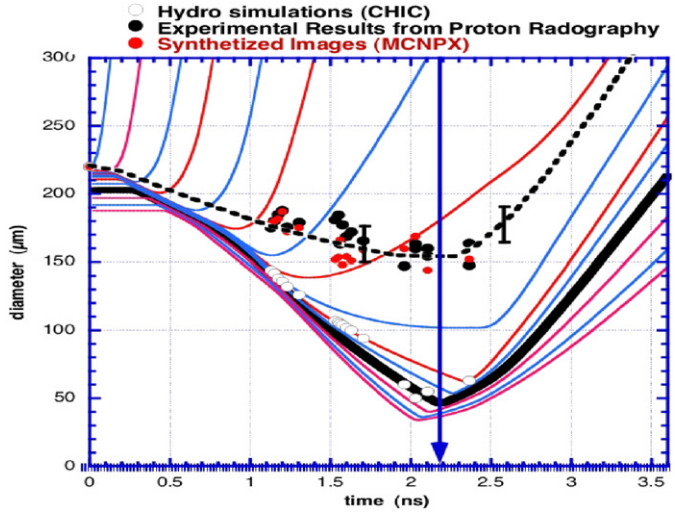

Figure 5. Comparison of experimental and simulation results. The point at 220 μm shows the initial diameter of the cylinder, empty circles show simulated results obtained running the hydro code CHIC, full ones the experimental points (dark on line) and the simulated results running the MCNPX MC code using hydrodensity profiles as input.

to MS effects. Figure 5 shows the comparison between experimental data and those obtained from synthetic images.

It is important to perform an analytical evaluation of MS, since this is considered to be the main effect responsible for the observed increase in the size of the proton images. This allows the real object size to be evaluated and also (as illustrated below) to evaluate the necessary conditions for obtaining good PR images. We can estimate the effect of MS on the *detected* size of the cylinder, by defining the blurring factor

$$\xi = L\vartheta; \qquad \vartheta = \frac{E_s}{2}\sqrt{\frac{1}{L_R}}\frac{\sqrt{A}}{E_p}; \qquad A = \int_{-\infty}^{\infty} \rho(x)\,\mathrm{d}x, \tag{1}$$

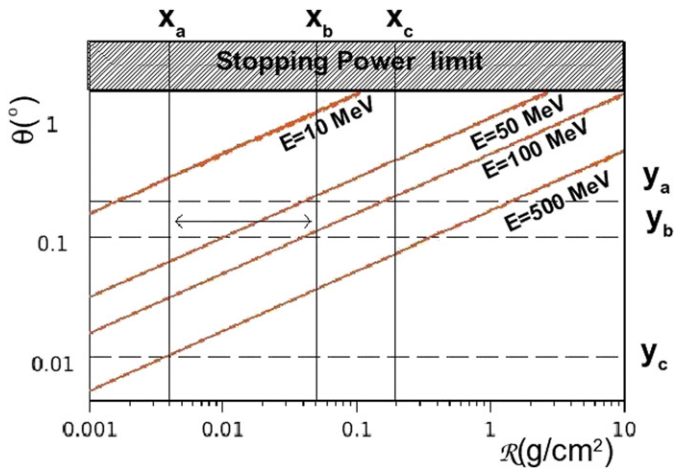

Figure 6. Mean scattering angle θ (equation (1)) versus areal density for different proton energies. (x_a) $R \sim 0.004\,\mathrm{g\,cm^{-2}}$ proton trajectory calculated through plasma corona and, (x_b) $R \sim 0.05\,\mathrm{g\,cm^{-2}}$ trajectory through core for the present experiment, (x_c) $R \sim 0.2\,\mathrm{g\,cm^{-2}}$ trajectory (theory) for a typical Omega target [19]. If we assume $d = L = 1$ cm we get the corresponding spatial resolution (equation (1)) limits: (y_a) $\sim$20 μm, (y_b) $\sim$10 μm, (y_c) $\sim$1 μm. The intersection between red (on line) and dashed lines represent the resolution reachable at that energy.

where L is the distance between the cylinder and the detector (figure 1), θ (rad) is the mean angular deflection [16] expected for a proton with energy E_p (MeV) traversing a material with a generalized area density A ($\mathrm{g\,cm^{-2}}$), $E_\mathrm{s} = 15$ MeV is a constant and L_r ($\mathrm{g\,cm^{-2}}$) is the radiation length. At each hydro-time point (i) the size D_i of the image formed on each RCF layer will be the convolution of the *real size* ϕ_ι of the cylinder image with the blurring coefficient ξ_i:

$$D_\mathrm{i} = \frac{1}{M}\sqrt{(\phi_\mathrm{i} M)^2 + \xi_\mathrm{i}^2}; \qquad M = \frac{d+L}{d}, \tag{2}$$

where M is the magnification factor and d the distance between the proton source and the target (figure 1). In principle, equations (2) can be inverted and an estimate of the *real* size of the cylinder for each time (t_i) obtained. In order to estimate the MS effect (equation (1)) the areal density A must be calculated; this is usually done, using a Gaussian approximation, as the peak density times the FWHM of the cylinder ($A \sim \rho L$). In this experiment the density profile is instead characterized, before stagnation, by three regions: (I) the plasma corona (low-density extended region), (II) the shocked region (which is compact and at high density) and (III) the unperturbed target (which remains at the original target density). Hence the proton traveling through the target will see the value of the peak density only over a short distance ($\sim$20 μm under our conditions). In this case, describing the entire target with a Gaussian approximation leads to an overestimation of the blurring coefficient. The areal density must be calculated instead by a detailed integration of the density profile across all three of the target regions identified above. Moreover, in this experiment the protons have a relatively low energy. The energy loss when they cross the target, and the multiple scattering effects are therefore quite large. In particular, the protons passing through the dense core of the imploded target are scattered more than protons passing through the external plasma corona, so the images are mainly formed by protons that have passed through less dense regions of the target. In this case the areal density in Rossi's formula should be calculated by integrating the density profile along the actual trajectories of the protons that are contributing to the image formation. Reference [4]

modeled the propagation of protons through the target using an algorithm based on the SRIM code [11], which is in principle quite similar to MCPNX. However, plasma effects were not taken into account, and analysis concentrated upon a single experimental image at fixed time neglecting the whole time evolution of the imploding target and the contributions from protons of different energies, i.e. they neglect image mixing mentioned in the above paragraph.

5. Resolution

A simple analytic criterion for measuring the resolution of PR can be obtained starting from the Rossi formula (1) assuming ξ/M as the resolution of the system, in analogy with Rayleigh's criterion in optics, and then by studying its variation as a function of the experimental parameters. In figure 5 typical values for the mean scattering angle versus areal density for different proton energies are shown for our experiment. The gray region corresponds to the ST limit, i.e. that of protons completely losing their energy inside the target.

6. Conclusion

PR has been used to diagnose the implosion of cylindrical targets, but a detailed analysis is required in order to allow comparison with hydro simulations. The simple RCF-layer-to-time relation does not hold here because of *image mixing*. The information carried by protons passing through the dense core is lost because these particles are scattered more than those passing through plasma corona. Those which are able to pass through other regions of the target are responsible for the formation of the images on detectors. Moreover, we have shown that under the conditions in which the experiment has been performed, ST is higher in low-density plasma than in cold matter. We have further shown how this can be taken into account in MC simulations. In any case, even if the time history and stagnation time are reproduced correctly, low-energy protons are not able to probe the dense core directly. MS is reduced for high-energy protons and, with respect to this problem, we have deduced a simple scaling law for proton energies to predict the minimum energy needed in order to reach acceptable resolution in ICF experiments.

Acknowledgment

The authors acknowledge the support of the HiPER project and Preparatory Phase Funding Agencies (EC, MSMT and STFC) in undertaking this work.

References

[1] Stott E, Wootton A, Gorini G and Batani D (ed) 2002 *Advanced Diagnostics for Magnetic and Inertial Fusion* (New York: Kluwer/Plenum)
[2] Li C K *et al* 2008 *Phys. Rev. Lett.* **100** 225001
[3] Rygg J R *et al* 2008 *Science* **319** 1223
[4] Mckinnon A J *et al* 2006 *Phys. Rev. Lett.* **97** 045001
[5] Borghesi M *et al* 2001 *Plasma Phys. Control. Fusion* **43** A267
[6] Dunne M *et al* 2007 *HiPER—Technical Background and Conceptual Design Report* Report RAL-TR-2007-008 (Didcot, UK: Rutherford Appleton Laboratory) available on the site www.Hiper-laser.org
[7] Perez F *et al* 2009 *Plasma. Phys. Control. Fusion* **51** 124035
[8] Volpe L *et al* 2011 *Phys. Plasmas* **18** 006101
[9] Borghesi M *et al* 2003 *Phys. Rev. Lett.* **82** 1529

[10] Batani D *et al* 2009 *Phys. Plasmas* **16** 1
[11] Fensin M L *et al* 2010 The enhancements and testing for the MCNPX 2.6.0 depletion capability *J. Nucl. Tech.* **170** 68–79 (Based on LA-UR-08-0305, https://mcnpx.lanl.gov)
Ziegler F *et al* 2009 The Stopping Power of Ions in Matter (Morrisville, NC: Lulu Press) available on the site www.srim.org
[12] Maire P H, Breil J, Abgral R and Ovadia J 2007 *SIAM SISC* **29** 1781
[13] Roth M *et al* 2002 *PRST Acc. Beams* **5** 061301
[14] GAFCHROMIC HD-810 Radiochromic Dosimetry Film and D-200 Pre-Formatted Dosimeters for High-Energy Photons Configurations (available on the site www.gafchromic.com/)
[15] Breschi E 2004 *Nucl. Instrum. Methods* A **522** 190
[16] Rossi B and Greisen K 1941 *Rev. Mod. Phys.* 13
[17] Mehlhorn T A 1981 *J. Appl. Phys.* **52** 6522
Peter T and Meyer-ter-Vehn J 1991 *Phys. Rev.* A **43** 4
[18] Young F C *et al* 1982 *Phys. Rev. Lett.* **49** 549
[19] LLE 2009 Annual Report October 2008 September 2009 DOGNA28503-923 January 2010 University of Rochester Laboratory for laser energetic